SCIENTIFIC REPORTS

OPEN

SUBJECT AREAS:
PHOTOCATALYSIS
NANOSCALE MATERIALS

Received
10 June 2014

Accepted
22 July 2014

Published
26 August 2014

Correspondence and requests for materials should be addressed to L.J. (Jinglq@hlju.edu.cn)

# Effective charge separation in the rutile $TiO_2$ nanorod-coupled $\alpha$-$Fe_2O_3$ with exceptionally high visible activities

Peng Luan, Mingzheng Xie, Dening Liu, Xuedong Fu & Liqiang Jing

Key Laboratory of Functional Inorganic Materials Chemistry (Heilongjiang University), Ministry of Education, School of Chemistry and Materials Science, Harbin 150080, P. R. China.

**Herein, we have fabricated rutile $TiO_2$ nanorod-coupled $\alpha$-$Fe_2O_3$ by a wet-chemical process. It is demonstrated that the visible activities for photoelectrochemical water oxidation and for degrading pollutant of $\alpha$-$Fe_2O_3$ are greatly enhanced after coupling a proper amount of rutile nanorods. The enhanced activity is attributed to the prolonged lifetime and improved separation of photogenerated charges mainly by the transient surface photovoltage responses. Interestingly, the observed EPR signals (with $g_{\perp} = 1.963$ and $g_{||} = 1.948$) of $Ti^{3+}$ in the fabricated $TiO_2$-$Fe_2O_3$ nanocomposite at ultra low temperature (1.8 k) after visible laser excitation, along with the electrochemical impedance spectra and the normalized photocurrent action spectra, testify evidently that the spacial transfers of visible-excited high-energy electrons of $\alpha$-$Fe_2O_3$ to $TiO_2$ could happen. Moreover, it is confirmed that it is more favorable for the uncommon electron transfers of $\alpha$-$Fe_2O_3$ to rutile than to anatase. This is responsible for the much obvious enhancement of visible activity of $Fe_2O_3$ after coupling with rutile $TiO_2$, compared with anatase and phase-mixed P25 ones. This work would help us to deeply understand the uncommon photophysical processes, and also provide a feasible route to improve the photocatalytic performance of visible-response semiconductor photocatalyst for water splitting and pollutant degradation.**

Solar energy, one of clean and environmentally friendly energy mode, is drawing more and more attention to meet the increasing demands in this century[1,2]. As a promising method, the photoelectrochemical (PEC) water splitting into $H_2$ and $O_2$ on semiconductor photoanode, it offers a solution to harvest and store solar energy[3–6]. Hematite ($\alpha$-$Fe_2O_3$) is currently considered one of the most promising photoanode materials for water splitting due to a series of desirable properties, including adequate absorption from the visible light region in solar spectrum (bandgap between 2.0 and 2.2 eV), high theoretical photocurrents under 1.5 AM illumination, excellent stability in an aqueous environment, and abundant existence in nature[4,7–9]. However, it usually exhibits weak photocatalytic performance for water splitting, mainly owing to the small absorption coefficient, the low carrier mobility and very short excited-state lifetime[10]. Hence, it is highly desired to enhance the photocatalytic performance of $Fe_2O_3$ for effective solar storage and utilization.

To improve the photocatalytic performance for water splitting of $Fe_2O_3$, enormous attempts have been focused on the development of controlled nanostructures[11,12], the modification on the surfaces[13,14], and the elemental doping[10,15]. Besides those attempts with certain successes, the heterojunctional composite construction between hematite and other semiconductor with a suitable energy-band structure is frequently employed[16]. It is generally acceptable that another semiconductor with lower conduction band bottom (CBB) level than $Fe_2O_3$ would be coupled to make photogenerated electrons transfer in space thermaldynamically, leading to the enhanced charge separation[17,18]. On the contrary, it seems impossible so that it is seldom reported to date. Surprisingly, it has been demonstrated in our recent work that the visible photocatalytic activity for $H_2$ production of $BiVO_4$ could be enhanced after coupling a proper amount of nanocrystalline anatase $TiO_2$[19], in which it is primarily suggested that the enhanced activities be attributed to the uncommon transfers of visible-excited electrons of $BiVO_4$ to anatase $TiO_2$.

Based on the energy band levels of $TiO_2$, $BiVO_4$ and $Fe_2O_3$[6], it is difficult to understand the suggested electron transfer processes. In fact, it is possible to allow to transfer enegetically since the high-energy electrons of $BiVO_4$ under visible irradiation could be produced. Unfortunately, it is lacking of evidences. Obviously, it is very meaningful for the uncommon electron transfers to effectively promote visible-excited charge sepatation of $\alpha$-$Fe_2O_3$ so as to enhance its photocatalytic activities. If it is a fact, it would also be applicable to other visible-

response semiconductor photocatalysts. Therefore, it is of great significance to testify the suggested uncommon electron transfers for effective visible photocatalysis from the points of scientific and engineering views.

It is well known that $TiO_2$ possesses wide energy bandgap so as to usually exhibit high photocatalytic activity under ultraviolet illumination in recent several decades[20]. It mainly exists as two polymorphs, anatase and rutile. Compared to anatase, rutile is relatively seldom investigated in the photocatalysis. However, it has two obvious advantages over anatase, high chemical stability and slightly-narrow energy bandgap[21]. Thus, it is expected that it is much favorable for the visible-excited electrons to transfer from $Fe_2O_3$ to rutile than to anatase. In addition, one-dimentional nanostructure is benificial to transport charges compared to zero-dimentional one[22]. Based on the above considerations, we try to fabricate rutile nanorod-coupled $\alpha$-$Fe_2O_3$, along with different-phase $TiO_2$-coupled ones in this work, aiming to clarify the suggested-above electron transfer process and its dependence on the titania phase composition.

## Results

**Structural characterization.** Based on the XRD patterns (Fig. 1A), along with the UV-Vis DRS spectra (SI-Fig. 1), it is confirmed that $\alpha$-$Fe_2O_3$, rutile $TiO_2$, and different mass contents of rutile $TiO_2$-coupled $\alpha$-$Fe_2O_3$ are obtained, and the optical absorption of $\alpha$-$Fe_2O_3$ across bang-gap energy does not change after coupling with a small amount of rutile $TiO_2$. It is seen from the TEM photograph (Fig. 1B) that the nanocrystalline $\alpha$-$Fe_2O_3$ is spherical-like with about 15 nm diameter[23], and the nanocrystalline rutile $TiO_2$ looks rod-like with 15 nm in width and 50 nm in length[24]. In particular, it is observed from the HRTEM image of circled area as the inset, in which the facet distances of 0.32 nm and 0.25 nm respectively correspond to rutile $TiO_2$ (110)[26] and $\alpha$-$Fe_2O_3$ (110)[27], that the connections between rutile nanorods and $\alpha$-$Fe_2O_3$ nanoparticles are intimate. In general, the intimate connnections are helpful for effective charge transfers among different constituents in the fabricated nanocomposite.

**Photogenerated charge properties.** The SS-SPS measurement, with a very high sensitivity, is a well-suitable and direct method to reveal the properties of photogenerated charges of solid semiconducting materials[25,29]. As for a nanosized semiconductor, its SPS response would mainly derive from the photogenerated charge separation via the diffusion process, since the formed band bending (or called built-in electric field) is neglectable. In general, the SPS response is greatly dependent on the $O_2$ concentration[28,29]. As shown in SI-Fig. 2A, no SPS response for $\alpha$-$Fe_2O_3$ is observed in the absence of $O_2$[30]. Differently, rutile $TiO_2$-coupled $\alpha$-$Fe_2O_3$ displays a detectable SS-SPS response in $N_2$ (SI-Fig. 2B), attributed to the photogenerated electron transfers from $\alpha$-$Fe_2O_3$ to $TiO_2$. It is clearly seen from Fig. 2A that, the $TiO_2$-coupled $\alpha$-$Fe_2O_3$ could display a strong SS-SPS response compared to $\alpha$-$Fe_2O_3$ in air, and it is the strongest for the 20RT-F. The strong SPS response frequently corresponds to the high photogenerated charge separation[31]. Noticeably, the $TiO_2$-coupled $\alpha$-$Fe_2O_3$ could exhibit a strong SS-SPS response in the visible range, also different from $TiO_2$. This could be explained by the strong visible absorption of $Fe_2O_3$ and its excited high-energy electron transfers to $TiO_2$. Naturally expected, the $TiO_2$-coupled $\alpha$-$Fe_2O_3$ would display a decreased SPS response if the amount of coupled $TiO_2$ is excess so as to be unfavorable for visible absorption. Hence, this ingenious tactic is feasible to reduce the visible-excited electron-hole recombination of narrow-gap $\alpha$-$Fe_2O_3$.

In particular, TS-SPV measurement is applied to investigate the dynamic processes of photogenerated charge carriers under a 532 nm laser excitation. For n-type $\alpha$-$Fe_2O_3$, its built-in electric field direction is from the inner to the outer in air, resulting in the charge enrichment of positive holes at the surfaces[31]. It is well known that, when the electron-hole pairs are generated in the space charge region of a semiconductor particle, they would be immediately separated under the built-in electric field, leading to the fast SPV component ($< 10^{-5}$ s). For n-type $Fe_2O_3$, its built-in electric field direction is from the inner to the outer in air. Therefore, its SPV signal should result from the charge enrichment of positive holes at the surfaces at the aid of built-in electric field. However, the diameter of a semiconductor nanoparticle is too small to build up a wide space-charge region, resulting into a weak fast SPV signal. Besides the built-in electric field, the charge separation is influenced by the carrier diffusion process, mainly contributing to the slow SPV response ($> 10^{-4}$ s)[32]. As shown in Fig. 2B, the $TiO_2$-coupled $\alpha$-$Fe_2O_3$ (20RT-F) exhibits a stronger TS-SPV response than $\alpha$-$Fe_2O_3$, which is in agreement with the SS-SPS result. Much prominently, the lifetime of photogenerated charge carriers of $\alpha$-$Fe_2O_3$ is obviously prolonged by several milliseconds. This indicates that the photogenerated charge separation of $\alpha$-$Fe_2O_3$ is greatly enhanced after coupling with rutile $TiO_2$ nanorods[19]. As expected, no TS-SPV response for $TiO_2$ is observed under visible laser excitement.

**Visible photocatalytic activities for water oxidation and pollutant degradation.** Based on the above SS-SPS and TS-SPV responses, it is confirmed that the photogenerated charge separation of $\alpha$-$Fe_2O_3$

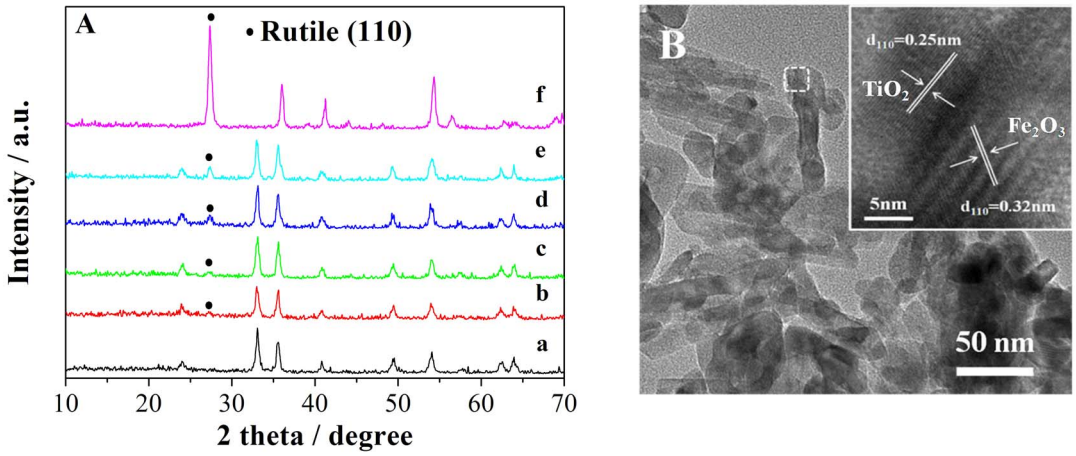


**Figure 1 | XRD patterns (A), and TEM image (20RT-F) with its HRTEM one from the selected area as the inset (B).** (a: F ($Fe_2O_3$), b: 10RT-F, c: 15RT-F, d: 20RT-F, e: 30RT-F, and f: RT (Rutile). X in the XRT-F nanocomposite means the mass content percentage of $TiO_2$, and the same elsewhere unless stated.)

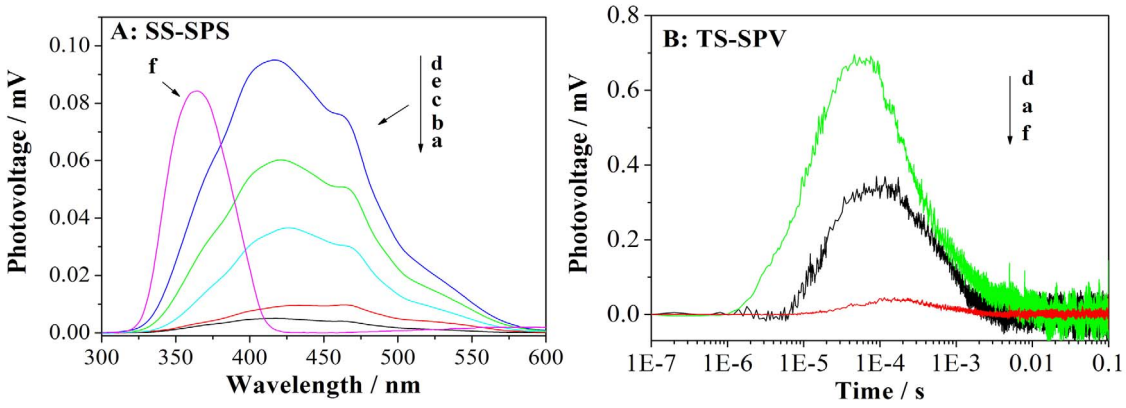


**Figure 2** | SS-SPS responses (A) and TS-SPV responses (B) in air.

could be greatly enhanced after coupling with a proper amount of rutile $TiO_2$ nanorods. As a result, it is naturally anticipated that its visible activities for PEC water oxidation and pollutant degradation would be markedly improved. One can see from SI-Fig. 3 that the dark scan displays almost negligible current density for all samples below 0.5 V. And also, the current onset of $\alpha$-$Fe_2O_3$ gradually shifts to the high potential (to that of $TiO_2$ as 0.7 V) as the amount of used $TiO_2$ is increased, illustrating that the coupled rutile $TiO_2$ would not be taken as cocatalysts for electrochemical water oxidation[13]. As shown in Fig. 3A, the photocurrent density of $\alpha$-$Fe_2O_3$ under visible irradiation gradually becomes large with increasing the amount of coupled $TiO_2$, and the 20RT-F sample exhibits the largest photocurrent density as 0.3 mA/cm$^2$ at 0.4 V vs Ag/AgCl, over 10-fold enhancement compared to $\alpha$-$Fe_2O_3$. If the amount of coupled $TiO_2$ is increased continuously, the photocurrent density of $TiO_2$-coupled $Fe_2O_3$ begins to become small. As expected, negligible current under visible illumination is detected for rutile $TiO_2$. Significantly, according to the inset of Fig. 3A, it is confirmed that the large photocurrent density corresponds to the large detector reading for produced $O_2$ in the PEC water oxidation[32,33].

The similar result is also obtained in the photocatalytic degradation of acetaldehyde (Fig. 3B). It is observed that the degradation rate of aldehyde on $\alpha$-$Fe_2O_3$ under visible irradiation could be increased after coupling with a proper amount of rutile $TiO_2$. This is also supported by the produced hydroxyl radical (·OH) amount as the inset. It is widely taken as a kind of active species in the photocatalytic process for ·OH[34]. The coumarin fluorescent method as a highly sensitive technique is widely used to detect the amount of ·OH, in which the introduced coumarin easily reacts with ·OH to produce luminescent 7-hydroxy-coumarin[31]. Noticeably, the strong fluorescence spectroscopy agrees with the high visible activity for degrading acetaldehyde.

## Discussion

Based on the above results, it is clearly demonstrated that the visible activities of $\alpha$-$Fe_2O_3$ for PEC water oxidation to evolve $O_2$ and pollutant degradation could be obviously improved after coupling with rutile $TiO_2$ nanorods, which is attributed to the greatly-promoted photogenerated charge separation. Why is the photogenerated charge separation enhanced? It is possibly related to the uncommon transfers of visible-excited high-energy electrons of $\alpha$-$Fe_2O_3$ to $TiO_2$. To verify the uncommon charge transfer process, we have carried out several experiments. Firstly, it is clearly seen from SI-Fig. 4A that the 20RT-F prepared by mechanically mixing exhibits a slightly lower SS-SPS response than $\alpha$-$Fe_2O_3$, responsible for the weak photocatalytic activity for degrading acetaldehyde (SI-Fig. 4B). This indicates that the weak connections between $\alpha$-$Fe_2O_3$ and $TiO_2$ are unfavorable for the effective charge transfers[35]. Secondly, on the basis of the electrochemical impedance spectra (Nyquist plots) of $\alpha$-$Fe_2O_3$ and $TiO_2$-coupled $\alpha$-$Fe_2O_3$ (20RT-F) in dark and under visible irradiation shown in Fig. 4A, it is noticed that the arc radius under visible irradiation is smaller than that in dark for two, especially for the 20RT-F one, attributed to the decreased charge-transfer resistance. Thus, it is deduced that the obviously-decreased charge-transfer resistance in 20RT-F results from the effective charge separation and transfer between the formed interfaces under visible irradiation[33].

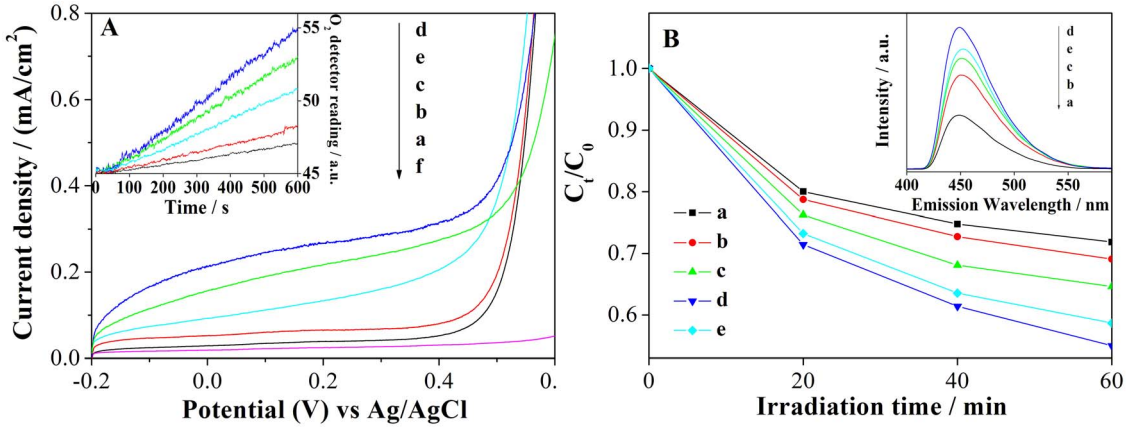


**Figure 3** | I-V curves in 1 M NaOH (pH=13.6) electrolyte under visible irradiation (A), with the temporal curves of produced $O_2$ in 0.5 M $Na_2SO_4$ electrolyte as the inset. Photocatalytic activity for degrading acetaldehyde under visible irradiation (B), along with the fluorescence spectra of the formed hydroxyl radical as the inset.

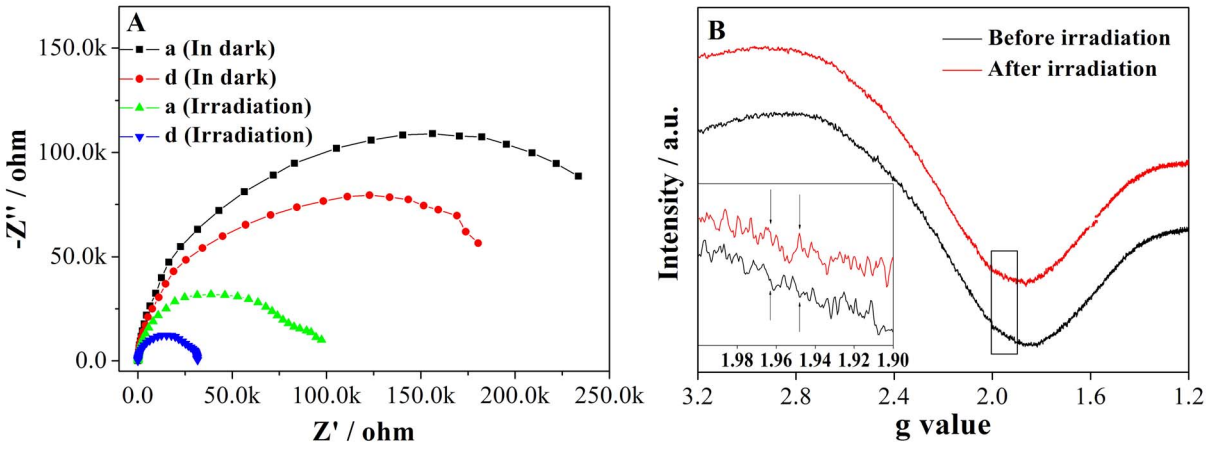


**Figure 4** | Electrochemical impedance spectra (EIS) were performed in dark and under visible irradiation at 0.4 V bias vs Ag/AgCl (A). Electron paramagnetic resonance (EPR) responses were measured at 1.8 K and the sample (20RT-F) was irradiated by one laser beam with wavelength of 532 nm (B).

Thirdly, we record the photocurrent densities of different layered film electrodes illuminated from the outer layer. It is observed from SI-Fig. 5 that the F/RT/FTO photoanode displays larger photocurrent density, compared with F/F/FTO and RT/RT/FTO ones, suggesting that the introduced rutile $TiO_2$ could promote the visible-excited charge separation of α-$Fe_2O_3$[36]. Lastly, also much importantly, the EPR method, widely employed[37,38], is also used to explore the processes of photogenerated charge transfer. In general, the EPR signal of $Ti^{3+}$ could be observed in rutile $TiO_2$ after band-gap excitation at low temperature, which is because that $Ti^{4+}$ would capture photogenerated electrons so as to produce $Ti^{3+}$[39]. Interestingly, it is noted from Fig. 4B that the EPR signal of $Ti^{3+}$, characterized by two sets of g values, $g_{\perp} = 1.969$ and $g_{||} = 1.947$[40], is detected in the $TiO_2$-coupled α-$Fe_2O_3$ (20RT-F) after visible laser excitation for 15 min. The detected $Ti^{3+}$ EPR signal indicates evidently that the transfer of visible-excited high-energy electrons from α-$Fe_2O_3$ to rutile $TiO_2$ could happen, leading to the $Ti^{3+}$ formation. In fact, it is not easy to observe the weak $Ti^{3+}$ signal, only at the ultra low temperature of 1.8 k (controlled by liquid helium) other than at the liquid-Nitrogen- and room- temperature.

On the basis of all the results mentioned above, the process schematic for charge transfer and separation in the fabricated nanocomposite is proposed in Fig. 5. It is clearly shown that the photogenerated electrons of α-$Fe_2O_3$ will be excited from VB to its different energy-level CB position under visible irradiation, including high-energy region (−0.05 eV ∼ −1.0 eV vs SHE) and low-energy region (0.1 eV ∼ −0.05 eV vs SHE) in this system[21]. Thus, the photogenerated electrons at low-energy level would quickly relax to the VB bottom of α-$Fe_2O_3$, then to recombine with holes. Differently, partial high-energy electrons would thermodynamically transfer to the CB of rutile $TiO_2$, leading to the prolonged lifetime and promoted separation of visible-excited charges[21]. This is further supported by the normalized photocurrent action spectra vs different excitation wavelength (Fig. 6) for α-$Fe_2O_3$, $TiO_2$-coupled α-$Fe_2O_3$ and rutile $TiO_2$. For α-$Fe_2O_3$, the photocurrent gradient keeps a relative-smooth variation with decreasing excitation wavelength. However, it is clearly seen for $TiO_2$-coupled α-$Fe_2O_3$ that there is a watershed at 550 nm for the photocurrent change, almost no change over 550 nm and gradual enhancement below 550 nm. This is in good accordance with the proposed charge transfers depending on the excitation wavelength. As expected, negligible photocurrent is for rutile $TiO_2$ under visible excitation (> 400 nm).

In the meantime, in order to investigate the effects of nanoparticle size of α-$Fe_2O_3$ on the charge transfer and separation, we synthesize different sizes of nanocrystalline α-$Fe_2O_3$ at different hydrothermal temperature and then fabricate different $TiO_2$-$Fe_2O_3$ nanocomposites at the same mass ratio to 20RT-F. According to the Scherrers equation by XRD patterns (SI-Fig. 6A), it is calculated that the average crystallite sizes of obtained α-$Fe_2O_3$ are 14.7, 19.8, 24.1 and 27.7 nm from low to high temperature, respectively. After introducing rutile $TiO_2$ (SI-Fig. 6B and 6C), the optical absorption of α-$Fe_2O_3$ is not distinctly changed. As seen from SI-Fig. 6D and SI-

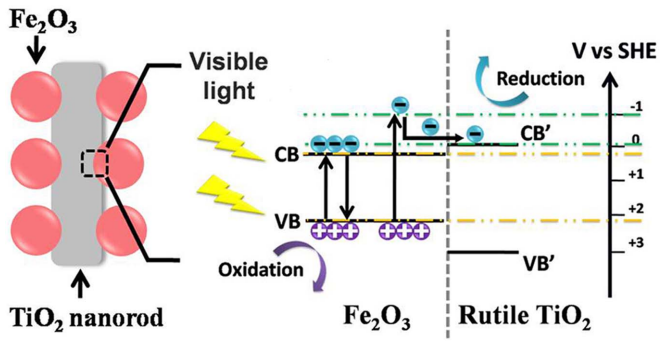


**Figure 5** | **Proposed process schematic of transfer and separation of visible-excited high-energy electrons in the fabricated $TiO_2$-$Fe_2O_3$ nanocomposite.** (CB: conduction band of $Fe_2O_3$, VB: valence band of $Fe_2O_3$. CB': conduction band of rutile $TiO_2$, VB': valence band of rutile $TiO_2$.)

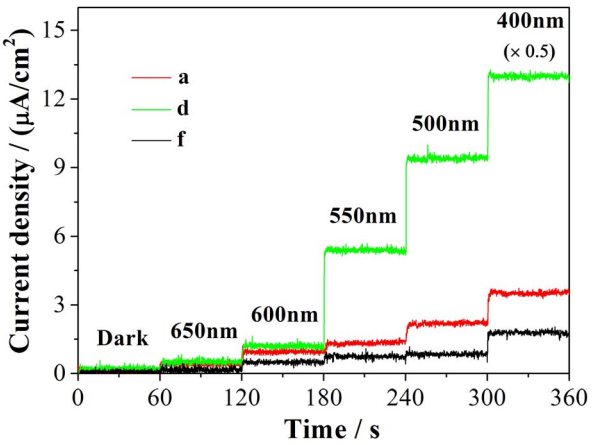


**Figure 6** | **Normalized photocurrent action spectra vs visible excitation wavelength at 0.4 V bias.**

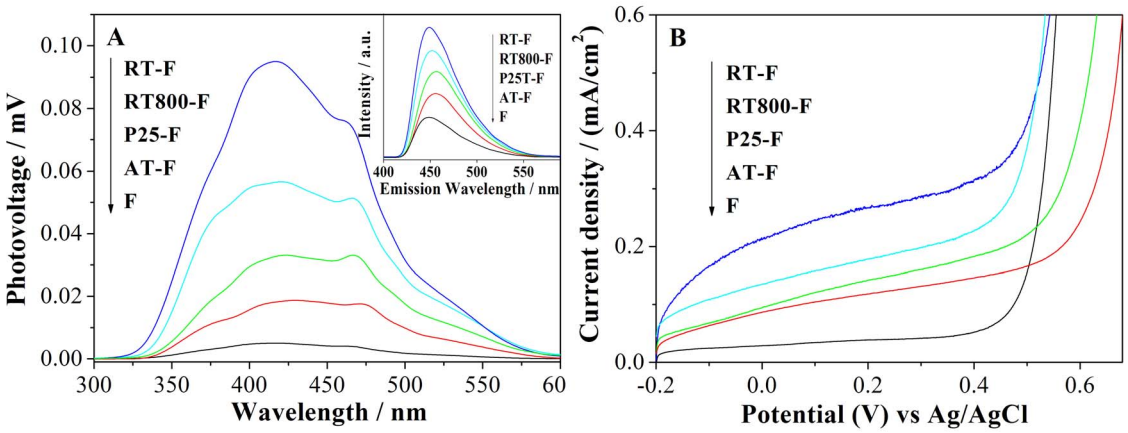


**Figure 7 | SS-SPS responses in air, with the fluorescence spectra for the formed hydroxyl radicals under visible irradiation as the inset (A), and I-V curves (B).** (AT: anatase obtained by sol-hydrothermal method, P25T: commercial $TiO_2$ produced by Degussa company, RT800: rutile obtained by calcining anatase at 800°C in air. AT-F: anatase $TiO_2$-coupled $Fe_2O_3$, P25T-F: P25 $TiO_2$-coupled $Fe_2O_3$, RT800-F: rutile $TiO_2$-coupled $Fe_2O_3$).

Fig. 6E, the small nanoparticle size of α-$Fe_2O_3$ corresponds to the strong SS-SPS response of resulting nanocomposite and its large photocurrent density under visible irradiation. This is because that the decreased nanoparticle size of α-$Fe_2O_3$ is favorable for the charge separation and for the formation of effective interface connects to transport charges[41,42].

Based on the process schematic shown in Fig. 5, it is speculated that the CB position of $TiO_2$ would provide with new level platforms for high-energy electrons, greatly influencing the charge transfer and separation. Thus, we explore the effects of $TiO_2$ CB positions on charge transfer and separation in nanocomposite by choosing different-phase-composition $TiO_2$, including anatase, phase-mixed and rutile $TiO_2$ with decreasing CB level (SI-Fig. 7A). One can see from SI-Fig. 7B and SI-Fig. 7C that the phase composition and the optical absorption of α-$Fe_2O_3$ do almost not change after coupling with different $TiO_2$. As shown in Fig. 7A, the SS-SPS responses of AT-F, P25T-F and RT800-F gradually become strong. Since it is well acceptable that the specific surface areas of nanocrystalline anatase and phase-mixed P25 $TiO_2$ are larger than that of rutile obtained by calcining nanocrystalline anatase at 800°C (SI- Fig. 8 and Table S1), it is elucidated for the strong SS-SPS response of RT800-F that the rutile phase possesses a slightly-low CB bottom (−0.05 eV) compared to anatase (−0.16 eV), so as to be much favorable to accept photogenerated electrons from $Fe_2O_3$. The SS-SPS result is also supported by the fluorescence spectra related to produced hydroxyl radical as the inset.

By comparison, it is confirmed from Fig. 7B that the strong SS-SPS response corresponds to the large photocurrent density under visible irradiation. Noticeably, the photocurrent density of 800RT-F is up to 0.23 mA/cm$^2$ at the bias potential of 0.4 V vs Ag/AgCl (1.4 V vs RHE), approximately 1.3 and 1.6 times larger than those of P25T-F and AT-F, respectively. In addition, the rutile $TiO_2$ nanorod-coupled $Fe_2O_3$ (20RT-F) exhibits stronger SS-SPS repsonse and larger photocurrent density than RT-800-F, which is close realted to its large surface area and nanorod structure favorable for charge transportation and separaton[43]. Hence, it is concluded that low CB position of rutile $TiO_2$ would greatly enable high-energy electrons to transfer in the nanocomposite system, as depicted in Fig. 8. To further testify the conclusion, we also record the normalized photocurrent action spectra from 600 to 500 nm at interval of 20 nm (SI-Fig. 9). It is observed that the photocurrent density of rutile-coupled $Fe_2O_3$ is always larger than that of anatase-coupled one, and it is much obvious for the excitaion wavelength below 560 nm, contributing to the produced high-energy electrons. This clearly indicates that the effective charge transfer greatly depends on the CB position of $TiO_2$.

In summary, we successfully fabricate rutile $TiO_2$ nanorod-coupled $Fe_2O_3$ through a wet-chemical method. It is demonstrated that the visible photocatalytic activities of α-$Fe_2O_3$ for splitting water to evolve $O_2$ and degrading pollutants could be greatly enhanced after coupling with a proper amount of rutile $TiO_2$ nanorod, attributed to the obviously prolonged lifetime and promoted separation of photogenerated charges. It is evidently comfirmed for the first time that the promoted charge separaion results from the uncommon transfers of visible-excited high-energy electrons of $Fe_2O_3$ to $TiO_2$ in the fabricated nanocomposite. In the case, the introduced $TiO_2$ provides with the energy platforms for produced high-energy electrons of α-$Fe_2O_3$. Moreover, it is more favorable for the uncommon electron transfers of α-$Fe_2O_3$ to rutile than to anatase, responsible for the much obvious enhancement of visible activity of $Fe_2O_3$ after coupling with rutile $TiO_2$, compared with anatase and phase-mixed P25 ones. This indicates that the uncommon electron transfer depends on the conduction band bottom level of $TiO_2$. This work would help us to deeply understand the uncommon photophysical processes, and also provide a feasible route to improve the photocatalytic performance of visible-response semiconductor photocatalyst for water splitting and pollutant degradation.

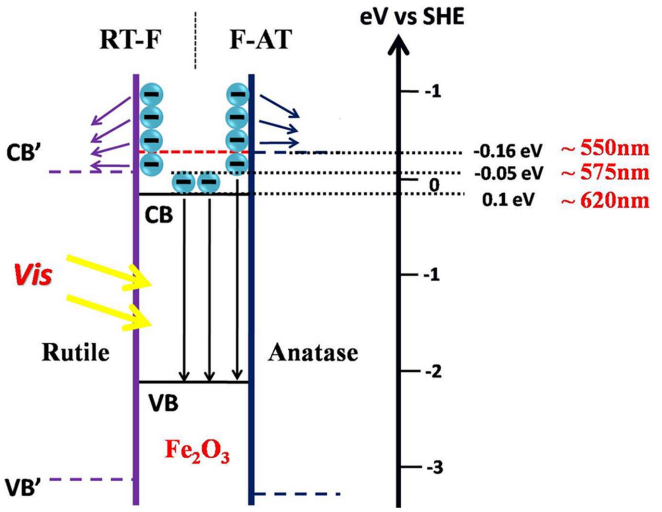


**Figure 8 | Schematic of visible-excited high-energy electron transfers in the fabricated nanocomposites based on the energy-band levels of anatase $TiO_2$, rutile $TiO_2$, and α-$Fe_2O_3$.** (CB': conduction band of rutile and anatase, VB': valence band of rutile and anatase. CB: conduction band of $Fe_2O_3$, VB: valence band of $Fe_2O_3$.)

## Methods

**Syntheses of materials.** $\alpha$-$Fe_2O_3$ was prepared by a water-organic two-phase separated hydrolysis-solvothermal (HST) method[23]. In a typical experiment, 10 mL water phase containing 0.5 mL ammonia and 8 mL n-butanol organic phase containing 0.8 g dissolved $Fe(NO_3)_3{\cdot}9H_2O$ were respectively placed in a 50 mL Teflon-lined stainless-steel vessel, in which a 10 mL weighing bottle was installed to contain the organic phase. Then, the sealed vessel was kept at 100°C for 6 h. The resulting $\alpha$-$Fe_2O_3$ was collected in the n-butanol after the autoclave was allowed to cool naturally to room temperature. After washed with deionized water and absolute ethanol in turn, and dried at 80°C in air, $\alpha$-$Fe_2O_3$ (F) nanoparticle was obtained.

Rutile $TiO_2$ nanorod was synthesized by a HCl-modified hydrothermal method[24]. Tetrabutyl titanate was used as the main starting material. Initially, this reagent was dropwise added to 2 mol/$L^{-1}$ concentrated hydrochloric acid (HCl) solution, maintained below 10°C by an ice-water bath. Then, the mixture was heated in a water bath for 4 h at 80°C so as to produce white suspension. Subsequently, the suspension was placed in Teflon-lined hydrothermal reactors and heated at 160°C for 6 h. After that, a white precipitate was collected, and then washed repeatedly with isopropanol and distilled water for five times to remove the adsorbed substances. After drying at 80°C in air, rutile $TiO_2$ (RT) was obtained.

To fabricate different mass ratios of $TiO_2$-coupled $Fe_2O_3$, we took the desired-amount of resulting $TiO_2$ and $\alpha$-$Fe_2O_3$ to put them together into a 50 mL of 50% ethanol solution under vigorously stirring for 1h. Subsequently, the mixture was heated to 85°C and kept the temperature under vigorously stirring. After evaporated out, the residual mixture was dried at 85°C in air. After thermal treatment at 450°C for 2 h, different $TiO_2$-$Fe_2O_3$ nanocomposites were obtained as XRT-F, in which X indicates the mass ratio of $TiO_2$ in the nanocomposite.

To compare with rutile $TiO_2$-coupled $Fe_2O_3$, we choose anatase, phase-mixed commercial P25 $TiO_2$, and another rutile $TiO_2$ to be respectively coupled to modify $\alpha$-$Fe_2O_3$ at the same mass ratio as 20RT-F by the similar wet-chemical processes. Anatase $TiO_2$ (spherical nanoparticle with 6 nm diameter) was synthesized by a sol-hydrothermal method at 200°C for 6 h in a Teflon-lined stainless-steel vessel[25]. The commercial P25 $TiO_2$ produced by Degussa company was purchased from the J&K company. Another rutile was obtained by traditionally calcining the obtained-above anatase $TiO_2$ at 800°C for 2 h. The as-prepared nanocomposites were accordingly defined as AT-F, P25T-F, and RT800-F, respectively.

**Characterization of materials.** The materials were characterized by X-ray Powder Diffraction (XRD) with a Rigaku D/MAX-rA powder diffractometer (Japan), using Cu K$\alpha$ radiation ($\alpha$= 0.15418 nm), and an accelerating voltage of 30 kV and an emission current of 20 mA were employed. The ultraviolet-visible diffuse reflectance spectra (DRS) of the samples were recorded with a Model Shimadzu UV2550 spectrophotometer. Transmission electron microscopy (TEM) observation was carried out on a JEOL JEM-2010EX instrument operated at 200 kV accelerating voltage. The nitrogen adsorption-desorption isotherms were measured by TriStar II 3020 at 77 K. And the specific surface area of the materials was calculated by the Brunauer–Emmett–Teller (BET) theory.

The steady-state surface photovoltage spectroscopy (SS-SPS) measurement of the sample was carried out with a home-built apparatus that has been described elsewhere[23–25]. Monochromatic light was obtained by passing light from a 500 W xenon lamp (CHFXQ500W, Global Xenon Lamp Power, made in China) through a double-prism monochromator (Hilger and Watts, D 300, made in England). A lock-in amplifier (SR830, made in U.S.A.), synchronized with a light chopper (SR540, made in U.S.A.), was employed to amplify photovoltage signal. The powder sample was sandwiched between two ITO glass electrodes, and the sandwiched electrodes were arranged in an atmosphere-controlled container with a quartz window for transmitting light.

The transient surface photovoltage (TS-SPV) measurement was performed with a self-assembled device in air atmosphere at room temperature, in which the sample chamber was connected to an ITO glass as the top electrode and to a steel substrate as the bottom electrode, and a 10 μm thick mica spacer was placed between the ITO glass and the sample to decrease the space charge region at the ITO-sample interface. The samples were excited by a 532 nm-laser radiation with 10 ns pulse width from a second harmonic Nd: YAG laser (Lab-130-10H, Newport, Co.). The laser intensity was modulated with an optical neutral filter and measured by a high energy pyroelectric sensor (PE50BF-DIF-C, Ophir Photonics Group). The TS-SPV signals were registered by a 1 GHz digital phosphor oscilloscope (DPO 4104B, Tektronix) with a preamplifier.

Electron paramagnetic resonance (EPR) measurement was conducted on a Bruker X-band (9.4 GHz) EMS plus 10/12 spectrometer. 2 mg $TiO_2$-coupled $\alpha$-$Fe_2O_3$ was dispersed in the glycerite (2 mL) and then transferred to an EPR tube. A cylindrical resonator (ER4119hs TE011) was used for data collection. A visible laser (532 nm, 5 W) was used as the light source. During the EPR data acquisition, the tube temperature was maintained at 1.8 K by an Oxford Instrument EPR 910 liquid helium continuous-flow cryostat. All the EPR data were collected at the High Magnetic Field Laboratory (Hefei City), Chinese Academy of Sciences.

**Photoelectrochemical (PEC) experiments.** PEC experiments were performed in a cubic quartz cell containing a pH 13.6 NaOH solution, using 500W Xenon lamp to produce a visible light source with an intensity of 64 mW/$cm^2$ after ultilizing a filter to remove light below the wavelength of 420 nm. Thus, the photocatalytic activity for water splitting was evaluated. The working electrode was the $TiO_2$-$Fe_2O_3$ nanocomposite film, irradiated from the FTO glass side. Platinum plate (99.9%) was used as the counter electrode, and a saturated-KCl Ag/AgCl electrode (SSE) was used as the reference electrode. All the potentials in the work were referred to SSE. Oxygen-free nitrogen gas was used to bubble through the electrolyte before and during the experiments. Applied potentials were controlled by a commercial computer-controlled potentiostat (AUTOLAB PG STAT 101). For comparison, the current was also measured on dark condition. Photocurrent density of different excitation wavelength was measured, in which monochromatic light was obtained by passing light from a 500 W xenon lamp through a monochromator (CM110, Spectral Produts). Electrochemical impedance spectra (EIS) were performed in a three-electrode configuration with the Princeton Applied Research Versa STAT 3 and carried out in the frequency range from $10^{-2}$ to $10^5$ Hz with amplitude of 10 mV (RMS) at the bias of 0.4 V in a 1.0 M NaOH solution, using 500W Xenon lamp to produce a visible light source with an intensity of 64 mW/$cm^2$ after ultilizing a filter to remove light below the wavelength of 420 nm.

To measure the produced $O_2$ amount in the PEC water oxidation, the as-prepared films were used as working electrodes in a sealed quartz cell with 0.5 M $Na_2SO_4$ solution of 80 mL as electrolyte, and high-purity nitrogen gas was employed to bubble through the electrolyte before the experiment. The films were illuminated from the FTO glass side, whose illuminated working area was about 0.5 cm × 0.5 cm, at the constant bias of 0.4 V. During the experiment, the produced $O_2$ amount was detected quantitatively with an Ocean Optics fluorescence-based oxygen sensor (NFSC 0058) by putting the needle probe into the electrolyte, near to the working electrode, and the irradiation was lasted for 10 min using 500W Xenon lamp to produce a visible light source with an intensity of 64 mW/$cm^2$ after ultilizing a filter to remove light below the wavelength of 420 nm.

**Photocatalytic activity evaluation.** Photocatalytic degradation of gas-phase acetaldehyde was conducted in a 640 mL of cylindrical quartz reactor with 3 mouths for introducing a planned amount of photocatalyst powders and a planned concentration of acetaldehyde gas. The reactor was placed horizontally and irradiated from the top side by using 500W Xenon lamp to produce a visible light source with an intensity of 64 mW/$cm^2$ after ultilizing a filter to remove light below the wavelength of 420 nm. In a typical photocatalytic process, 0.2 g of photocatalyst was used, and a premixed gas system, which contained 800 ppm acetaldehyde, 20% of $O_2$, and 80% of $N_2$, was introduced into the reactor. To reach adsorption saturation, the mixed gas continuously moved through the reactor for 0.5 h prior to the irradiation. The determination of acetaldehyde concentrations at different time intervals in the photocatalysis was performed with a gas chromatograph (GC-2014, Shimadzu) equipped with a flame ionization detector.

In the analysis of hydroxyl radical, 50 mg sample and 20 mL 5 mg/$L^{-1}$ coumarin aqueous solution were fixed in a 50 mL quartz reactor. Using 500W Xenon lamp to produce a visible light source with an intensity of 64 mW/$cm^2$ after ultilizing a filter to remove light below the wavelength of 420 nm, which is placed at about 10 cm from the reactor under magnetically stirring for 1 h. Finally, a certain amount of the solution was transferred into a Pyrex glass cell for the fluorescence measurement of 7-hydroxycoumarin under the light excitation of 332 nm.


1. Lewis, N. S. & Nocera, D. G. Powering the planet: Chemical challenges in solar energy utilization. *Proc. Natl. Acad. Sci. U. S. A.* **103**, 15729–15735 (2006).
2. Chen, X. B., Shen, S. H., Guo, L. J. & Mao, S. S. Semiconductor-based Photocatalytic Hydrogen Generation. *Chem. Rev.* **110**, 6503–6570 (2010).
3. Grätzel, M. Photoelectrochemical cells. *Nature* **414**, 338–344 (2001).
4. Walter, M. G. *et al.* Solar Water Splitting Cells. *Chem. Rev.* **110**, 6446–6473 (2010).
5. Zhang, J. S. *et al.* Photocatalytic oxidation of water by polymeric carbon nitride nanohybrids made of sustainable elements. *Chem. Sci.* **3**, 443–446 (2012).
6. Li, Z. S., Luo, W. J., Zhang, M. L., Feng, J. Y. & Zou, Z. G. Photoelectrochemical cells for solar hydrogen production: current state of promising photoelectrodes, methods to improve their properties, and outlook. *Energy Environ. Sci.* **6**, 347–370 (2013).
7. Zhong, D. K., Sun, J., Inumaru, H. & Gamelin, D. R. Solar Water Oxidation by composite Catalyst/$\alpha$-$Fe_2O_3$ Photoanodes. *J. Am. Chem. Soc.* **131**, 6086–6087 (2009).
8. Lin, Y. J., Yuan, G. B., Sheehan, S., Zhou, S. & Wang, D. W. Hematite-based solar water splitting: challenges and opportunities. *Energy Environ. Sci.* **4**, 4862–4869 (2011).
9. Hamann, T. W. Splitting water with rust: hematite photoelectrochemistry. *Dalton Trans.* **41**, 7830–7834 (2012).
10. Franking, R. *et al.* Facile post-growth doping of nanostructured hematite photoanodes for enhanced photoelectrochemical water oxidation. *Energy Environ. Sci.* **6**, 500–512 (2013).
11. Lian, J. B. *et al.* J. Hematite ($\alpha$-$Fe_2O_3$) with Various Morphologies: Ionic Liquid-Assisted Synthesis, Formation Mechanism, and Properties. *ACS Nano* **11**, 3749–3761 (2009).
12. Tilley, S. D., Cornuz, M., Sivula, K. & Grätzel, M. Light-Induced Water Splitting with Hematite: Improved Nanostructure and Iridium Oxide Catalysis. *Angew. Chem. Int. Ed.* **49**, 6405–6408 (2010).
13. Zhong, D. K., Cornuz, M., Sivula, K., Grätzel, M. & Gamelin, D. R. Photo-assisted electrodeposition of cobalt–phosphate (Co–Pi) catalyst on hematite photoanodes for solar water oxidation. *Energy Environ. Sci.* **4**, 1759–1764 (2011).

14. Jing, L. Q. *et al.* Dynamics of photogenerated charges in the phosphate modified $TiO_2$ and the enhanced activity for photoelectrochemical water splitting. *Energy Environ. Sci.* **5**, 6552–6558 (2012).
15. Wang, G. M., Yang, X. Y., Qian, F., Zhang, J. Z. & Li, Y. Facile Synthesis of Highly Photoactive α-$Fe_2O_3$-Based Films for Water Oxidation. *Nano Lett.* **10**, 1088–1092 (2010).
16. Mayer, M. T., Lin, Y. J., Yuan, G. B. & Wang, D. W. Forming heterojunctions at the nanoscale for improved photoelectrochemical water splitting by semiconductor materials: case studies on hematite. *Acc. Chem. Res.* **46**, 1558–1566 (2013).
17. Hong, S. J., Lee, S., Jang, J. S. & Lee, J. S. Heterojunction $BiVO_4$/$WO_3$ electrodes for enhanced photoactivity of water oxidation. *Energy Environ. Sci.* **4**, 1781–1787 (2011).
18. Kim, E. S. *et al.* Fabrication of $CaFe_2O_4$/TaON Heterojunction Photoanode for Photoelectrochemical Water Oxidation. *J. Am. Chem. Soc.* **135**, 5375–5383 (2013).
19. Xie, M. Z. *et al.* Long-Lived, Visible-Light-Excited Charge Carriers of $TiO_2$/$BiVO_4$ Nanocomposites and their Unexpected Photoactivity for Water Splitting. *Adv. Energy Mater.* available online, DOI: 10.1002/aenm. 201300995 (2013).
20. Chen, X. B. & Mao, S. S. Titanium Dioxide Nanomaterials: Synthesis, Properties, Modifications, and Applications. *Chem. Rev.* **107**, 2891–2959 (2007).
21. Naya, S., Kimura, K. & Tada, H. One-Step selective aerobic oxidation of amines to imines by gold nanoparticle-loaded rutile titanium(IV) oxide olasmon photocatalyst. *ACS Catal.* **3**, 10–13 (2013).
22. Hwang, Y. J., Hahn, C., Liu, B. & Yang, P. D. Photoelectrochemical Properties of $TiO_2$ Nanowire Arrays: A Study of the Dependence on Length and Atomic Layer Deposition Coating. *ACS Nano* **6**, 5060–5069 (2012).
23. Sun, W. T., Meng, Q. Q., Jing, L. Q., Liu, D. N. & Cao, Y. Facile Synthesis of Surface-Modified Nanosized α-$Fe_2O_3$ as Efficient Visible Photocatalysts and Mechanism Insight. *J. Phys. Chem C* **117**, 1358–1365 (2013).
24. Luan, Y. B. *et al.* Synthesis of efficient nanosized rutile $TiO_2$ and its main factors determining its photodegradation activity: roles of residual chloride and adsorbed oxygen. *J. Phys. Chem. C* **116**, 17094–17100 (2012).
25. Jing, L. Q., Qu, Y. C., Su, H. J., Yao, C. H. & Fu, H. G. Synthesis of High-Activity $TiO_2$-Based Photocatalysts by Compounding a Small Amount of Porous Nanosized $LaFeO_3$ and the Activity-Enhanced Mechanisms. *J. Phys. Chem. C* **115**, 12375–12380 (2011).
26. Andersson, M., Kiselev, A., Österlund, L. & Palmqvist, A. E. C. Microemulsion-Mediated Room-Temperature Synthesis of High-Surface-Area Rutile and Its Photocatalytic Performance. *J. Phys. Chem. C* **111**, 6789–6797 (2007).
27. Chen, J. S., Zhu, T., Yang, X. H., Yang, H. G. & Lou, X. W. Top-Down Fabrication of α-$Fe_2O_3$ Single-Crystal Nanodiscs and Microparticles with Tunable Porosity for Largely Improved Lithium Storage Properties. *J. Am. Chem. Soc.* **132**, 13162–13164 (2010).
28. Jing, L. Q., Zhou, W., Tian, G. H. & Fu, H. G. Surface tuning for oxide-based nanomaterials as efficient photocatalysts. *Chem. Soc. Rev.* **42**, 9509–9549 (2013).
29. Cao, Y. *et al.* Enhanced photocatalytic activity of nc-$TiO_2$ by promoting photogenerated electrons captured by the adsorbed oxygen. *Phys. Chem. Chem. Phys.* **14**, 8530–8536 (2012).
30. He, L. M., Jing, L. Q., Li, Z. J., Sun, W. T. & Liu, C. Enhanced visible photocatalytic activity of nanocrystalline α-$Fe_2O_3$ by coupling phosphate-functionalized grapheme. *RSC Adv.* **3**, 7438–7444 (2013).
31. Peng, L. L., Xie, T. F., Lu, Y. C., Fan, H. M. & Wang, D. J. Synthesis, photoelectric properties and photocatalytic activity of the $Fe_2O_3$/$TiO_2$ heterogeneous photocatalysts. *J. Phys. Chem. Chem. Phys.* **12**, 8033–8041 (2010).
32. Tang, J. W., Durrant, J. R. & Klug, D. R. Mechanism of Photocatalytic Water Splitting in $TiO_2$. Reaction of Water with Photoholes, Importance of Charge Carrier Dynamics, and Evidence for Four-Hole Chemistry. *J. Am. Chem. Soc.* **130**, 13885–13891 (2008).
33. Hou, Y., Zuo, F., Dagg, A. & Feng, P. Y. Visible Light-Driven α-$Fe_2O_3$ Nanorod/Graphene/$BiV_{1-x}Mo_xO_4$ Core/Shell Heterojunction Array for Efficient Photoelectrochemical Water Splitting. *Nano Lett.* **12**, 6464–6473 (2012).
34. Nakabayashi, Y. & Nosaka, Y. OH Radical Formation at Distinct Faces of Rutile $TiO_2$ Crystal in the Procedure of Photoelectrochemical Water Oxidation. *J. Phys. Chem. C* **117**, 23832–23839 (2013).
35. Dekrafft, K. E., Wang, C. & Lin, W. B. Metal-Organic Framework Templated Synthesis of $Fe_2O_3$/$TiO_2$ Nanocomposite for Hydrogen Production. *Adv. Mater.* **24**, 2014–2018 (2012).
36. Saito, R., Miseki, Y. & Sayama, K. Highly efficient photoelectrochemical water splitting using a thin film photoanode of $BiVO_4$/$SnO_2$/$WO_3$ multi-composite in a carbonate electrolyte. *Chem. Commun.* **48**, 3833–3835 (2012).
37. Priebe, J. B. *et al.* Water Reduction with Visible Light: Synergy between Optical Transitions and Electron Transfer in Au-$TiO_2$ Catalysts Visualized by In situ EPR Spectroscopy. *Angew. Chem. Int. Ed.* **52**, 11420–11424 (2013).
38. Huang, J. *et al.* Highly Efficient Ultrafast Electron Injection from the Singlet MLCT Excited State of Copper(I) Diimine Complexes to $TiO_2$ Nanoparticles. *Angew. Chem. Int. Ed.* **124**, 12883–12887 (2012).
39. Konovalova, T. A. & Kispert, L. D. Surface Modification of $TiO_2$ Nanoparticles with Carotenoids. EPR Study. *J. Phys. Chem. B* **103**, 4672–4677 (1999).
40. Kumar, C. P., Gopal, N. O., Wang, T. C., Wong, M. & Ke, S. C. EPR Investigation of $TiO_2$ Nanoparticles with Temperature-Dependent Properties. *J. Phys. Chem. B* **110**, 5223–5229 (2006).
41. O'Regan, B. C. *et al.* Measuring Charge Transport from Transient Photovoltage Rise Times. A New Tool To Investigate Electron Transport in Nanoparticle Films. *J. Phys. Chem. B* **110**, 17155–17160 (2006).
42. Park, K., Zhang, Q. F., Myers, D. & Cao, G. Z. Charge Transport Properties in $TiO_2$ Network with Different Particle Sizes for Dye Sensitized Solar Cells. *ACS Appl. Mater. Interfaces* **5**, 1044–1052 (2013).
43. Hou, Y., Zuo, F., Dagg, A. & Feng, P. Y. A Three-Dimensional Branched Cobalt-Doped α-$Fe_2O_3$ Nanorod/$MgFe_2O_4$ Heterojunction Array as a Flexible Photoanode for Efficient Photoelectrochemical Water Oxidation. *Angew. Chem. Int. Ed.* **52**, 1248–1252 (2013).


## Acknowledgments

We are grateful for financial support from NSFC (21071048), the Program for Innovative Research Team in Chinese Universities (IRT1237), the Research Project of Chinese Ministry of Education (213011A), the Specialized Research Fund for the Doctoral Program of Higher Education (20122301110002), the Chang Jiang Scholar Candidates Programme for Heilongjiang Universities (2012CJHB003), and the Science Foundation for Excellent Youth of Harbin City of China (2014RFYXJ002). A special thank is given to Dr. Wei Tong from High Magnetic Field Laboratory (Chinese Academy of Sciences, Hefei 230031, China) for support in EPR measurements and discussion.

## Author contributions

L.Q.J. planned the project, and P.L. and D.N.L. carried out experiments and data analyses. M.Z.X. and X.D.F. contributed to the SS-SPS and TS-SPV measurements and photocatalytic $H_2$ evolution test. All the authors participated in discussion of the research. P.L. and L.Q.J. wrote the paper.

## Additional information

**Supplementary information** accompanies this paper at http://www.nature.com/scientificreports

**Competing financial interests:** The authors declare no competing financial interests.

**How to cite this article:** Luan, P., Xie, M., Liu, D., Fu, X. & Jing, L. Effective charge separation in the rutile $TiO_2$ nanorod-coupled α-$Fe_2O_3$ with exceptionally high visible activities. *Sci. Rep.* **4**, 6180; DOI:10.1038/srep06180 (2014).

This work is licensed under a Creative Commons Attribution-NonCommercial-ShareAlike 4.0 International License. The images or other third party material in this article are included in the article's Creative Commons license, unless indicated otherwise in the credit line; if the material is not included under the Creative Commons license, users will need to obtain permission from the license holder in order to reproduce the material. To view a copy of this license, visit http://creativecommons.org/licenses/by-nc-sa/4.0/